

Research Article

Energy Dissipation Contribution Modeling of Vibratory Behavior for Silicon Micromachined Gyroscope

J. Zhou,^{1,2} Q. Shen ,^{1,3} J. B. Xie ,^{1,3} P. P. Cao,⁴ and W. Z. Yuan³

¹Research & Development Institute of Northwestern Polytechnical University in Shenzhen, China

²Northwestern Polytechnical University, Xi'an, China

³The MOE Key Laboratory of Micro and Nano Systems for Aerospace, Northwestern Polytechnical University, Xi'an 710072, China

⁴Shanghai Institute of Radio Equipment, Shanghai 200090, China

Correspondence should be addressed to Q. Shen; shenqiang1917@126.com

Received 25 January 2018; Accepted 6 March 2018; Published 14 June 2018

Academic Editor: Md Abdul Halim Miah

Copyright © 2018 J. Zhou et al. This is an open access article distributed under the Creative Commons Attribution License, which permits unrestricted use, distribution, and reproduction in any medium, provided the original work is properly cited.

Energy dissipation contribution of micro-machined Coriolis vibratory gyroscope (MCVG) is modeled, numerically simulated, and experimentally verified in this paper. First, the amount of independent damping dissipation consisting of thermoelastic loss, anchor loss, surface loss, Akhiezer loss, and air damping loss during vibration is obtained by simulation model, PML-based method, and numerical calculation, respectively. Then, temperature and pressure dependence characteristic of the corresponding quality factor (Q) for the MCVG are obtained. Meanwhile, dominant sources of damping dissipation are determined, which paves the way to improve Q. Finally, the temperature-dependent and pressure-dependent characteristics of the total Q are measured with errors of less than 10% and 18% compared with the simulated total Q, respectively, in which accuracy is acceptable for predicting the damping dissipation behavior of MCVG in design stage before high-cost fabrication.

1. Introduction

Vibration behavior is an important feature of MEMS two-order mass-damping-stiffness system. Energy conversion is a fundamental characteristic of these vibrational system. For some type MEMS devices, vibration regarded as energy is collected as power of electrical components, such as vibration energy harvest [1–3]. For another type devices, this vibration behavior can be localized to improve signal noise ratio (SNR) greatly [4]. Nevertheless, more common but inevitable phenomenon for all of MEMS devices during vibration occurrence is vibration energy dissipation behavior, typically such as micromachined Coriolis vibratory gyroscope (MCVG) [5–7]. The performance of this type of vibration system is significantly limited by the rate at which the vibration energy is dissipated, which is called time constant. Q is generally used as a measurement of this time constant of the vibration energy and is defined as ratio of the total strain energy to the dissipated energy per vibration cycle. Higher Q means larger time constant and lower vibration energy dissipation, for the

MCVG, which means achievement of excellent bias stability [8–12].

In order to achieve high performance of the MCVG, analysis of energy dissipation mechanisms of the Q value of the MCVG during vibration becomes an important issue [13–16]. For the single-mode mass-damping-stiffness resonator, the Q value has been widely regarded as a combination of five energy dissipation mechanisms and inverse proportion to the total energy dissipation [17–19]. Energy dissipation usually consists of two categories: intrinsic dissipation such as thermoelastic damping loss $1/Q_{the}$, anchor damping loss $1/Q_{anc}$, and Akhiezer damping loss $1/Q_{akh}$ and extrinsic dissipation such as surface damping loss $1/Q_{sur}$ and air damping loss $1/Q_{air}$.

These damping loss mechanisms of the single-mode resonators have been extensively investigated for achieving the expected Q. In summary, influencing factors on damping losses can contribute to three aspects: vacuum packaging technology, materials properties, and mechanical structure topology. First, vacuum packaging scheme as the

most common one is used to greatly decrease air damping, such as *epi-seal* encapsulation process [20–25], hermetic lid sealing process [13, 26–28], Through-Silicon Via (TSV) process [29, 30], and SPIL MEMS WLP process [31]. Second, some different kinds of materials are tried to yield lower the thermoelastic, surface deflect, and Akhiezer damping. For example, crystalline and doped silicon are chosen frequently to make high-Q resonators because of their excellent semiconductor properties [32–37]. Researchers also take advantage of single crystal (SC) [38], microcrystalline (MC) [39–42], nanocrystalline (NC) [43, 44], and ultra NC [45] diamonds to achieve high-Q resonators by trading off contributions of different damping loss items, respectively. As for the structure topologies which mainly affect anchor damping, anchor loss models of simple cantilever beam have been established [46–48]. However, for some complex fully 3D resonators, contributions of another geometrical resonators including DETF [21], tether geometry [49–51], microsphere [52], cupped [52, 53], wineglass [54], hemispherical [39], and disk shapes [55–57] to anchor loss are calculated hard by the analytical solution if no simplifying assumption is present. Damping loss model on accurately estimating the experiment results for these complex structure topology is very limited. Main reason is that it is difficult to obtain precise a priori knowledge of the stress profile at the anchor area of these design. Especially for the MCVG with both the drive and sense modes, the elastic beams connecting with anchors exist mechanical vibration coupling between the drive and sense modes.

Therefore, we will try to model and simulate the energy dissipation mechanisms for MCVG by numerical analysis technologies in this paper. Furthermore, the contribution of each damping dissipation to the total quality factor of the MCVG is predicted. The experiments are also implemented to verify the theoretical analyzes.

This paper is organized as follows: in Section 2, modeling and simulation of the independent damping dissipation for the MCVG are presented. In Section 3, temperature and pressure dependence characteristic measurements of the quality factor are implemented. Finally, the conclusions are provided in Section 4.

2. Numerical Simulation Analysis of Damping Dissipation

Here, we consider our single-mass z-axis MCVG as the example to [8, 58–60] to analyze the contribution of the damping loss, as shown in Figure 1. The symmetrical SOI-based MCVG structure consists of a set of the electrodes, anchors, elastic beams, and three masses including the drive-mode mass, the sense-mode mass, and the proof mass. The structure is fixed on the substrate through four anchors, which connect with eight elastic beams. The vibration between both modes is decoupled through eight other elastic beams located at the proof mass. In order to enhance the performance, Q value of the MCVG should be as high as possible.

2.1. Contribution Of Damping Dissipation. According to Zener's theory [17, 18], for the MCVG, the contribution of all

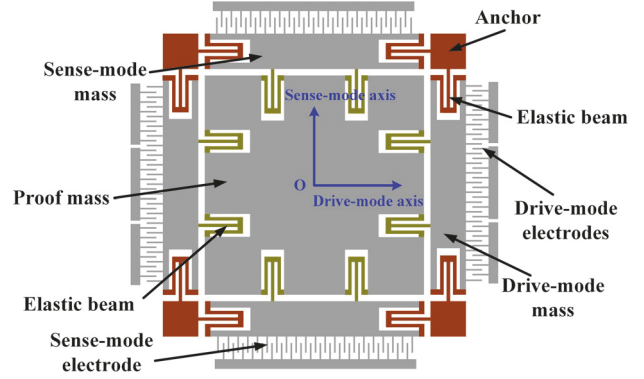


FIGURE 1: The schematic of the simulated MCVG.

the damping losses items to the total quality factor Q_t can be further expressed as

$$\frac{1}{Q_t} = \frac{1}{Q_{the}} + \frac{1}{Q_{anc}} + \frac{1}{Q_{sur}} + \frac{1}{Q_{akh}} + \frac{1}{Q_{air}} \quad (1)$$

where Q_{the} , Q_{anc} , Q_{sur} , Q_{akh} , and Q_{air} represent the quality factor related to thermoelastic damping loss, anchor damping loss, surface deflect damping loss, Akhiezer damping loss, and air damping loss.

2.1.1. Thermoelastic Damping Loss. Thermoelastic damping is part of mechanical vibration energy dissipated in the form of heat energy. This type of damping loss exists in the place of the mechanical structure deformation caused by elastic strain. It depends closely on geometric size and material property of the structure. For the simple mechanical structure such as cantilever beam, analysis solution of thermoelastic damping has been obtained fairly accurately. However, for the MCVG, the accurate analysis solution is deduced hardly because of the existing coupled elastic vibration between the drive and sense mode. So, finite element model of the thermoelastic damping is established. Then, the thermoelasticity modulus in Comsol software is used to extract Q_{the} by solving the coupled mechanical and thermal differential equations. The detailed calculation process is demonstrated as follows.

The first step is the finite element model of the MCVG established in Comsol and then the elastic vibration is simulated to obtain the elastic stain tensor ζ_{xy} at any point inside the structure and stored maximum vibration energy W .

The second step is to obtain transient temperature ∇T of the MCVG by heat transfer simulation. $\nabla = \partial i/\partial x + \partial j/\partial y + \partial k/\partial z$ is Hamilton operator. The above elastic stain is first substituted into the expression $T_0 \zeta_{xy} (c_{11} + 2c_{12}) \alpha$ [19] regarded as internal heat source, where T_0 is initial temperature of 20°C, c_{11} and c_{12} are the second-order elastic stiffness tensors, and α is tensor of the thermal expansion. Then, transient temperature ∇T of the MCVG internally is simulated by the thermoelastic modulus.

The last step is to derive Q_{the} during the mechanical structure vibration. Considering heat transfer in the mechanical structure made from a thermally isotropic material of single

TABLE 1: GEOMETRICAL PARAMETER AND MATERIAL PROPERTIES.

Parameters	Value	units
Length of middle elastic beams	440	μm
Length of boudary elastic beams	420	μm
Width of middle elastic beams	12	μm
Width of boundary elastic beams	8	μm
Area of each anchor	1500×1500	μm^2
Area of proof mass	4000×4000	μm^2
Area of drive/sense mode mass	4000×800	μm^2
Resonance frequency f	4000	Hz
Specific heat, C	700	J/kg/K
Density, ρ	2329	kg/m^3
Thermal conductivity, K	130	W/m/K
Young's modulus, E	169	GPa
Coefficient of thermal expansion, α	2.6e-6	1/K
Thermal diffusivity	7.97e-5	m^2/s

crystal silicon, increment rate \dot{S}_{tot} of the total entropy yielded from the thermal conduction of the internal heat source can be written as

$$\dot{S}_{tot} = - \int_V \frac{q \cdot \nabla T}{T^2} dV \quad (2)$$

where $q = \kappa \cdot \nabla T$ is the heat flux and κ is thermal conductivity coefficient. dV is small volume element during vibration. According to the thermodynamics theory, heat amount increment dQ produced during vibration can be written as

$$dQ = T \times dS_{tot} = \int \frac{\kappa \cdot \nabla T^2}{T} dV \quad (3)$$

Further, heat amount increment ΔQ during a period t_s of vibration can be written as

$$\Delta Q = T \times dS_{tot} = \int_0^{t_s} \int_0^V \frac{\kappa \cdot \nabla T^2}{T} dV dt \quad (4)$$

According to the above vibration energy W , quality factor Q_{the} caused by thermoelastic dissipation can be obtained as follows:

$$Q_{the} = 2\pi \frac{W}{\Delta Q} \quad (5)$$

According to Figure 1, geometrical parameters of the single crystal silicon (SCS) MCVG and the material parameters are first listed in Table 1.

Through setting the parameters listed in Table 1, energy loss distribution of the thermoelastic damping for the MCVG is obtained at the initial temperature of 20°C , as shown in Figure 2. It can be seen that the thermoelastic damping loss mainly exists at connection region between the mass and the elastic beams in both of the modes; meanwhile, the rest of the thermoelastic loss occurs at the anchors region connecting the elastic beams. This means that higher strain gradient exists in these regions, where temperature gradient is caused and further generates the thermal flow.

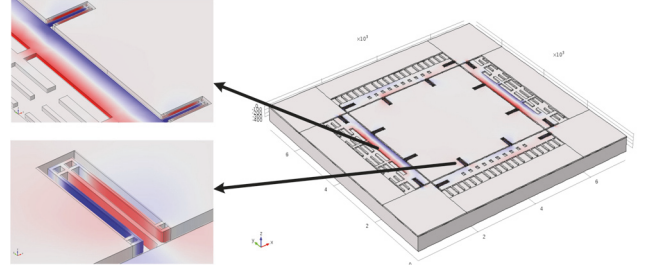


FIGURE 2: Energy distribution of thermoelastic damping of the MCVG at the temperature of 20°C .

Further, Q_{ted} within the temperature of -40°C to 60°C is simulated. Due to the SCS properties variation with temperature such as E , K , C , and α , the material properties as a function of temperature are set in the thermoelasticity modulus of Comsol. Figure 3 shows Q_{the} of thermoelastic damping versus temperature.

It can be seen from Figure 3 that Q_{the} caused by thermoelastic damping is five orders of magnitude, reaching about 0.3 million. Further, Q_{the} decreases gradually with temperature rising. When temperature is 20°C , Q_{the} is 241000.

2.1.2. Anchor Damping Loss. Anchor damping is part of elastic-beam vibration energy radiated and dissipated into the substrate in the form of elastic wave. Perfectly matched layers (PML-based) method is induced to calculate Q_{anc} of anchor damping in this work. Berenger first introduced the PML concept to analyze an issue on electromagnetic propagation in 1994 [61]. Recently, Bindel applied the PML to estimate the anchor loss of 2D MEMS device [62]. However, analytical solution of anchor loss Q_{anc} for the fully 3D structure is still hard to achieve until now. So, we try to estimate the anchor damping Q_{anc} by establishing the PML-based numerical model of the MCVG.

Figure 4 shows the finite element model (FEM) of the MCVG using a PML to model the substrate as a finite space by

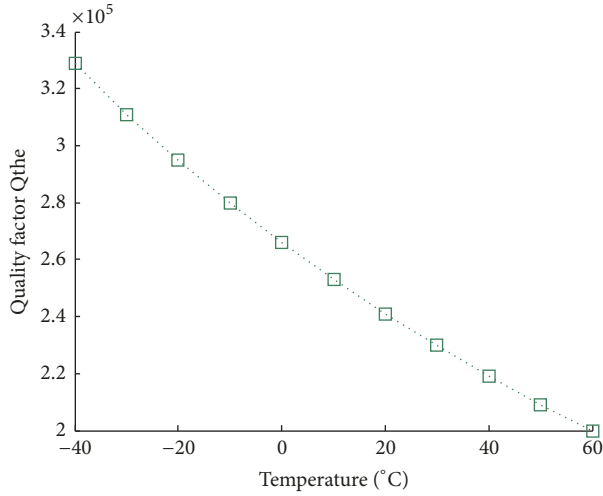


FIGURE 3: Q_{the} as a function of temperature.

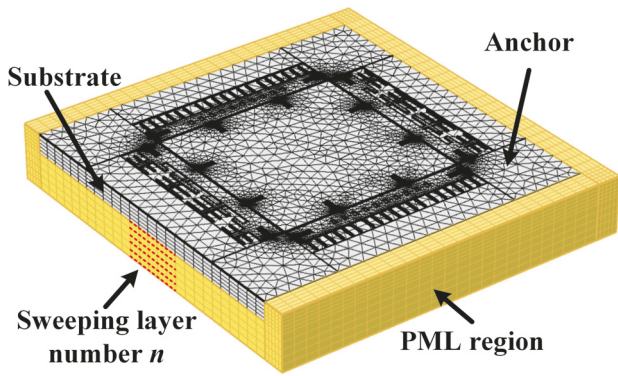


FIGURE 4: FEM of the MCVG using PML substrate as finite space marked in yellow.

solid mechanics module in the Comsol. The MCVG locates on the PML substrate. According to the PML theory, PML field is demanded as far away from the strong gradient field at the attachment of the MCVG to the substrate. Mesh grids of the PML are divided in the sweeping form. Theoretically, thickness of each sweeping meshing layer in the PML should be less than one-third of elastic wavelength jointly determined by the wave velocity and the resonance frequency of the MCVG. So, sweeping meshing layer number n becomes critical for the estimation accuracy of anchor damping Q_{anc} . With the sweeping layer number n increasing, the estimated Q_{anc} is more accurate, whereas computational cost rises sharply. Material parameters of the PML are same as that of the substrate layer of the MCVG.

Figure 5 shows the PML-based elastic wave simulation results of the anchor damping. It can be seen that the elastic waves propagate into the substrate through the connection between the elastic beams and anchors. The occurrence of the elastic waves is mainly caused by the elastic beams deformation during vibration, which gives rise to stress at the connection area. Finally, this vibration energy as the anchor loss is dissipated through the elastic wave propagation in

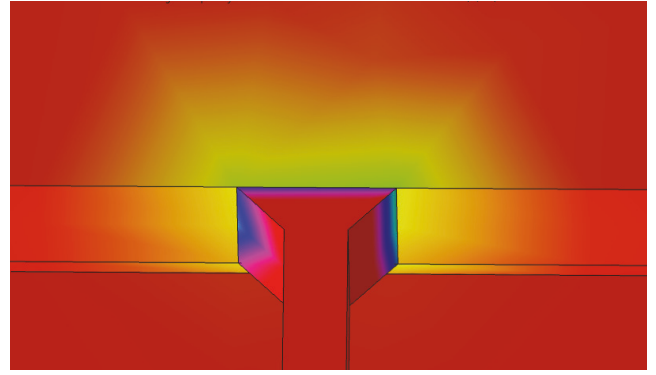


FIGURE 5: PML-based energy propagation of the anchor damping at the connection between the beam and anchor.

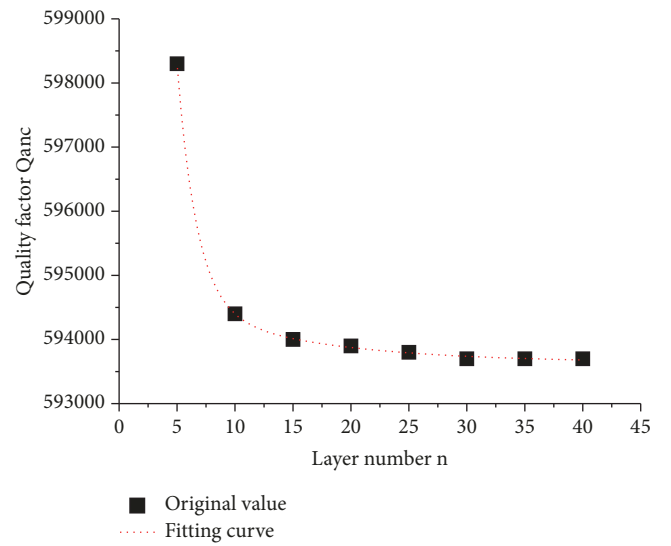


FIGURE 6: Estimated Q_{anc} versus sweeping layer number n .

the PML substrate. According to the above analysis, anchor dissipation can be reduced by the following ways. One is to locate the beams connecting with anchor at the center of mass to decrease deformation degree of the beams. The other is to reduce the total number of the beams connecting with anchors to decrease energy dissipation.

Figure 6 plots anchor damping Q_{anc} versus the sweeping layer number n at the initial temperature of 20°C . Q_{anc} is an exponential function of the sweeping layer number by fitting the scatter spots. When the number n increases from 5 to 15, Q_{anc} decreases significantly. This means that estimation accuracy of Q_{anc} is a bit low. Nevertheless, with n further increasing, Q_{anc} approximately keeps constant, reaching 593700. Its estimation accuracy is significantly improved. Nevertheless, computational cost of PC work station rises sharply. Further, the estimated anchor damping Q_{anc} is a little larger than the thermoelastic damping Q_{the} .

2.1.3. Surface Damping Loss. The surface damping is related to the surface layer conditions of the structure such as the surface contamination and deformation induced during

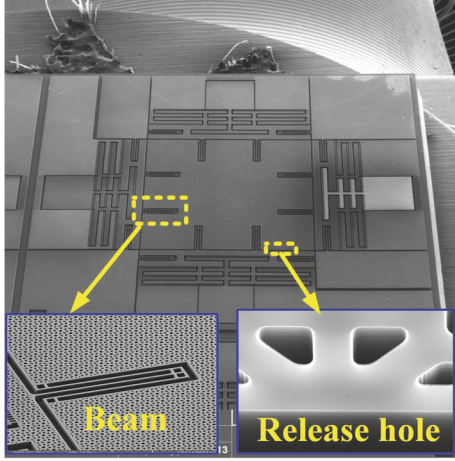


FIGURE 7: SEM of the MCVG.

the fabrication process [47, 63]. For the MCVG, first of all, adsorbates on the surface layer can be fully cleaned up by careful operation in the clean room, as shown in Figure 7. Second, when the MCVG vibrates along the drive axis, the surface deformation of the proof mass is negligible because of its large rigid body characteristic, although lots of tiny release roles distribute in the proof mass. So, surface layer deformation only occurs on the elastic beams. It is further regarded as surface damping loss caused by the layer deformation which is given rise solely by the beams deformation. Nevertheless, because the ratio reaching 0.001 between the surface of the beams and the volume of the proof mass is that small, as shown in Figure 7, surface damping loss caused by the surface deformation of the beams can be also neglected for the MCVG.

2.1.4. Akhiezer Damping Loss. Akhiezer damping loss [21] happens when the period of the MCVG vibration is slower than inelastic phonon scattering process, which mainly restores the local thermal equilibrium disturbed by strain during the vibration of the single crystal. This loss is related to the strain caused by acoustic wave propagation process within the silicon material. Quality factor Q_{akh} induced by the Akhiezer damping can be estimated as follows:

$$Q_{akh} = \frac{\rho c^4}{2\pi\gamma_{avg}^2 K f} \times \frac{1}{T} \quad (6)$$

where ρ , f , K , and T are density of single crystal silicon, resonance frequency of the MCVG, thermal conductivity, and temperature, respectively. c , γ_{avg} , and K are acoustic velocity within the silicon material and average Grünesen's coefficient, which are equal to 1.04×10^5 m/s and 0.51, respectively. Q_{akh} is inversely proportional to temperature. When the temperature is set as 20°C , Q_{akh} is calculated to be 1.09×10^{11} . Compared with the thermoelastic and anchor damping, Akhiezer damping is so small that its effect to quality factor can be neglected.

2.1.5. Air Damping Loss. Air damping is part of extrinsic energy dissipation occurring on the moving surface of the device. The pressure determined by the vacuum level of the device cavity has significant influence on estimation of this damping. For the MCVG, the surface movement mainly occurs between the fixing comb fingers and moving comb fingers, bottom surface of the proof mass, and the substrate, respectively. Quality factor Q_{air} of the MCVG can be obtained by calculating as follows.

First, mean free path of air molecules in the MCVG cavity can be written as

$$\lambda = \frac{k_B T}{\sqrt{2}\pi d^2 P} \quad (7)$$

where P is air pressure in the cavity and Boltzmann constant k_B and effective diameter of air molecule d are equal to 1.38×10^{-23} J/K and 3×10^{-10} m, respectively. Due to slipping effect of air existing on the moving surface, air viscosity coefficient μ should be modified as its effective value μ_{eff} [64]

$$\mu_{eff} = \frac{\mu}{1 + 2K_n + 0.2K_n^{0.788} e^{-K_n/10}} \quad (8)$$

where μ is equal to 1.8×10^{-5} Pa·s at the temperature of 20°C , Knudsen number K_n is equal to λ/D . and D is gap between the adjacent comb fingers and the bottom surface layer of the proof mass and the substrate layer, which are $2\mu\text{m}$ and $5\mu\text{m}$, respectively. Then, damping coefficient c_{dmp} is obtained as follows:

$$c_{dmp} = \frac{\mu_{eff} A}{D} \quad (9)$$

where A are area between the adjacent comb fingers and the bottom surface layer of the proof mass and the substrate layer, which are $30\mu\text{m} \times 10\mu\text{m}$ and $4000\mu\text{m} \times 4000\mu\text{m}$, respectively. Through the calculation, sum of the damping coefficients c_{dmp_cmb} between the comb fingers and c_{dmp_mass} between the bottom surface and the substrate is 4.51×10^{-7} N/m/s. According to the equation $Q_{air} = m_d \times 2\pi f \times (c_{dmp_cmb} + c_{dmp_mass})$, where m_d is sum of the drive-mode mass and proof mass, Q_{air} induced by air damping is calculated to reach 56345 at the temperature of 20°C and pressure of 10Pa. Further, quality factor Q_{air} as a function of pressure P at the temperature of 20°C is plotted in log scales in Figure 8.

It can be seen from Figure 8 that quality factor Q_{air} is approximately linear with pressure P in log scales. Quality factor increases with pressure decreasing. Further, temperature dependence of the quality factor Q_{air} is investigated. According to [65], viscosity coefficient μ versus temperature T can be written as

$$\mu = \mu_0 \frac{384}{T + 111} \left(\frac{T}{273} \right)^{1.5} \quad (10)$$

where viscosity coefficient μ_0 is 1.71×10^{-5} Pa·s at the temperature of 0°C . Putting (8) and (10) to (9), through calculation, Q_{air} as a function of temperature at the pressure of 10Pa is plotted in Figure 9.

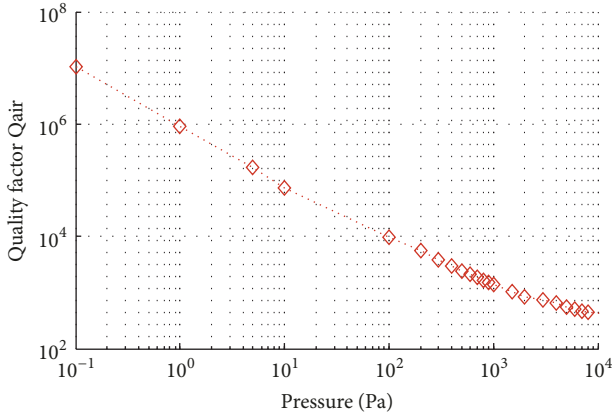


FIGURE 8: Quality factor Q_{air} versus pressure P at the temperature of 20°C .

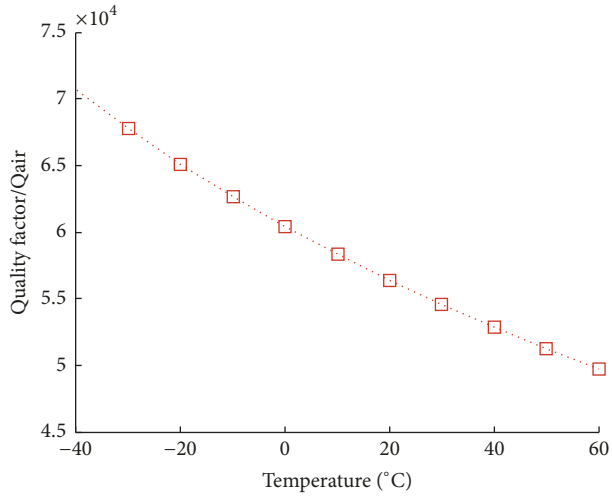


FIGURE 9: Quality factor Q_{air} versus temperature T at the pressure of 10Pa .

TABLE 2: QUALITY FACTOR OF DAMPING DISSIPATION.

	Quality factor	Value	Percentage of $1/Q$
Intrinsic dissipation	Q_{the}	241000	17.60%
	Q_{anc}	593700	7.14%
	Q_{akh}	1.09×10^{11}	≈ 0
Extrinsic dissipation	Q_{sur}	/	/
	Q_{air}	56345	75.26%
Total dissipation	Q_{tot}	42405	/

In Figure 9, with temperature increasing, Q_{air} decrease gradually, which keeps in the order of $\sim 10^4$ within the temperature of -40°C to 60°C .

According to (1), contribution of the damping dissipations to the quality factor at the pressure 10Pa and temperature of 20°C can be listed in Table 2.

It can be seen that the total quality factor at the given condition of temperature and pressure is 42405 . The damping

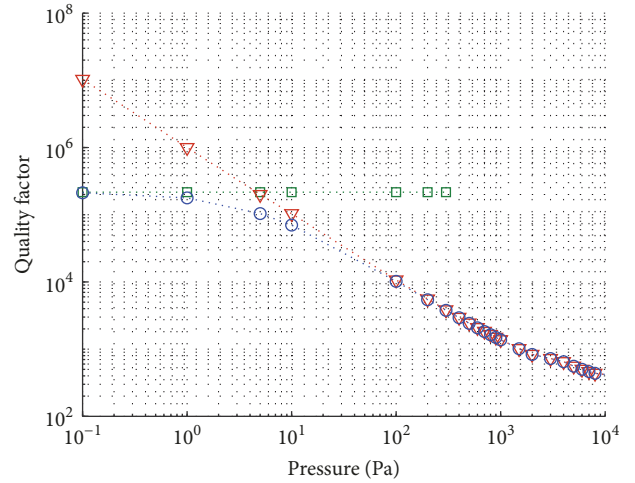


FIGURE 10: Total quality factor Q_{tot} versus pressure P at the temperature of 20°C .

dissipation is mainly determined by the thermoelastic damping, anchor damping, and air damping, which is a dominant source of dissipation, reaching 75.26% .

2.2. Pressure-Dependent Characteristic of Quality Factor. Due to pressure-independent characteristic of the thermoelastic, anchor, and Akhiezer damping, these three quality factors are approximately constant over the pressure. Considering (1) and Figure 8, total quality factor Q_{tot} versus pressure P can be calculated, as shown in Figure 10.

It can be seen that the total quality factor Q_{tot} tends to be constant, reaching the order of 10^5 , when the pressure level is lower than 5Pa . This means that the thermoelastic damping and anchor damping are dominant sources of dissipation within this range of pressure level. When the pressure level is beyond 5Pa , the relatively low Q_{tot} approaches Q_{air} , which implies that air damping become dominant dissipation source. Further, the simulated Q_{tot} is about 42405 at the pressure level of 10Pa .

2.3. Temperature-Dependent Characteristic of Quality Factor. Due to weak temperature-independent characteristic of the anchor damping [21], Q_{anc} is approximately regarded as be constant over the temperature. Considering (1) and Figures 3 and 8, total quality factor Q_{tot} versus temperature T at the pressure of 10Pa can be calculated, as shown in Figure 11.

It can be seen that the total quality factor Q_{tot} decreases slowly from 52978 to 37313 with temperature increasing, which approximately keeps in the order of $\sim 10^5$ at the pressure level of 10Pa . Q_{tot} varies 15665 within the temperature range of -40°C to 60°C . The simulated Q_{tot} is 42405 at the temperature of 20°C . Further, Q_{tot} is close to Q_{air} . This means that the air damping is dominant source of dissipation at this pressure level.

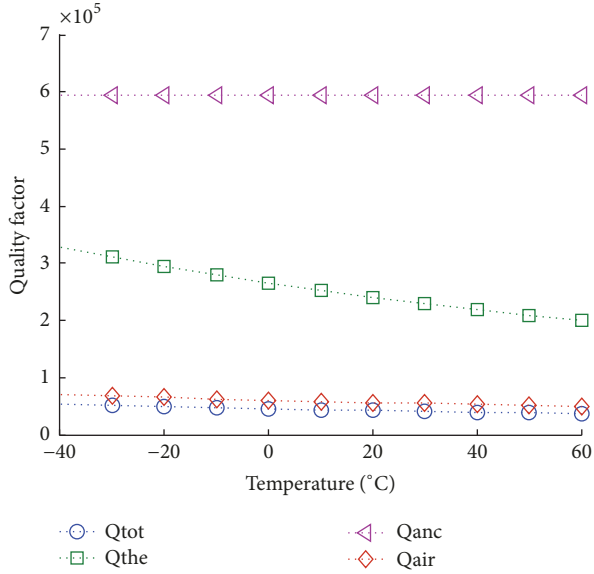


FIGURE 11: Quality factor Q_{tot} versus temperature T at the pressure of 10Pa.

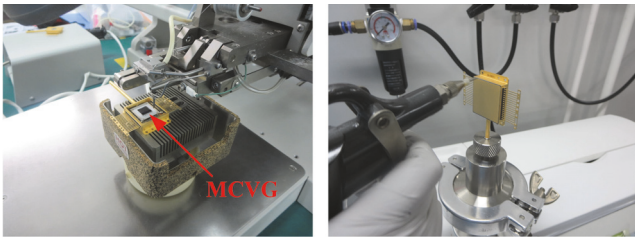


FIGURE 12: MCVG on the packaging platform.

3. Measurement and Comparison

The presented MCVG is packaged on the vacuum operation platform, as shown in Figure 12. The packaging pressure is 10Pa. First, Q_{tot} as a function of temperature T is tested in the temperature controlling chamber, as shown in Figure 13. Q_{tot} of three gyroscopes are calibrated by using the 3dB bandwidth method, respectively.

The measured Q_{tot} is plotted by the scatter spots, as shown in Figure 14. It can be seen that the measured total Q_{tot} of the three gyroscopes decreases with temperature increasing at the pressure level of 10Pa. Their change trend is almost consistent. The error bars represent accuracy of the measured values of Q_{tot} . The average value of the Q_{tot} of three gyroscopes reaches 49040 at the 40°C, 39116 at the 60°C, and 41087 at the 20°C. Compared with the simulated results shown in Figure 11, errors at these corresponding temperature spots are 7.4%, 4.8%, and 3.1%, respectively. In the whole temperature range, the error is all less than 10%, which means that the numerical simulation of the quality factor versus temperature for the MCVG is acceptable for predicting the quality factor characteristic.

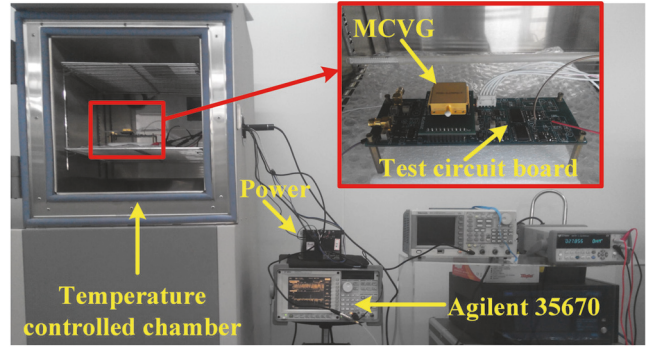


FIGURE 13: Test system of Q_{tot} versus temperature.

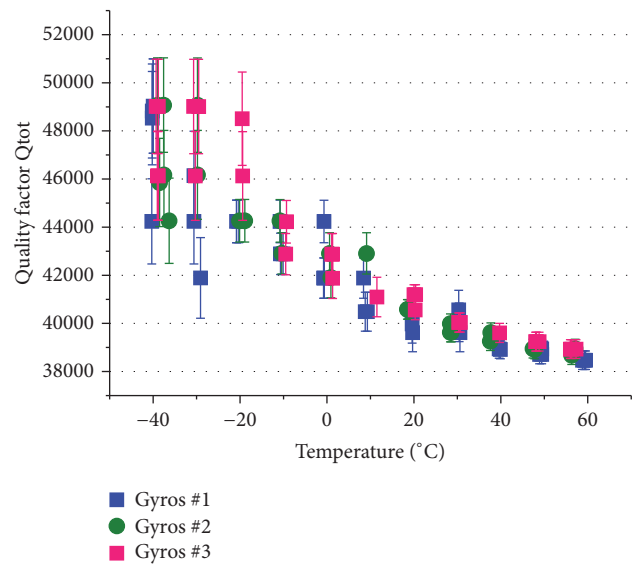


FIGURE 14: Measured quality factor Q_{tot} with temperature T changing at the pressure of 10Pa.

After the temperature dependence experiment of quality factor for the vacuum-packaged MCVG, the cover of the metal package is opened and the exposed MCVG is then put into the vacuum exhaust chamber to implement the pressure-dependent experiment of the quality factor, as shown in Figure 15.

Through controlling the pressure in the exhaust chamber, pressure-dependent characteristic of Q_{tot} is obtained when the temperature is 20°C. Test data is plotted by the scatter spots, as shown in Figure 16.

In the pressure range from 0.017Pa to 3000Pa, the measured Q_{tot} increases slowly when the pressure is reduced from 5Pa to 0.017Pa, reaching the maximum value of 95872, which means that Q_{the} and Q_{anc} are dominant sources of damping dissipation. Nevertheless, Q_{tot} drops inversely to 511 when the pressure is beyond 10Pa. Q_{tot} is 34766 at the pressure level of 10Pa with an error of 18% compared with the simulated Q_{tot} . Overall, the measured Q_{tot} is relatively a little small, whereas both of their trends keep consistent. The error between the

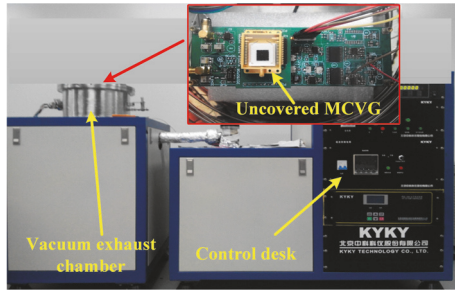


FIGURE 15: Test system of Q_{tot} versus pressure.

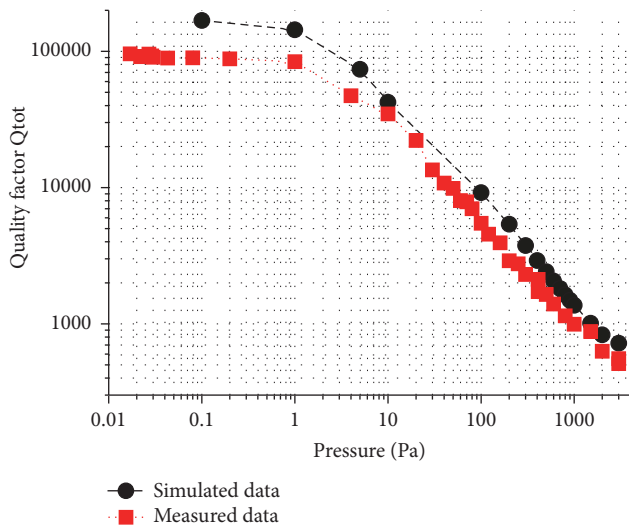


FIGURE 16: Measured quality factor Q_{tot} with pressure P at the temperature of 20°C .

simulation data and measurement data may be mainly caused by uncertain material property and measurement accuracy.

4. Conclusions

In this paper, the energy dissipation contributions of the quality factor of the MCVG during vibration are established and verified experimentally. Some conclusions can be obtained. First, the thermoelastic damping and anchor damping dominate the quality factor of MCVG when the pressure level is less than 5 Pa. Corresponding Q of these two damping reach the order of 10^5 , and Q_{the} is a little less than Q_{anc} . Nevertheless, air damping becomes dominant dissipation source with the pressure level beyond 5 Pa. Second, temperature dependence characteristic of the total Q is dominated by air damping dissipation when the pressure keeps at the level of 10 Pa. It can be also predicted that contribution of the thermoelastic damping and anchor damping to temperature dependence characteristic of total Q becomes larger with the pressure level decreasing. Last, the practical measurements prove that the error of the established damping dissipation model could predict the quality factor of the MCVG with an acceptable error.

Data Availability

The data used to support the findings of this study are available from the corresponding author upon request

Conflicts of Interest

The authors declare that there are no conflicts of interest regarding the publication of this paper.

Acknowledgments

This work was supported in part by JCYJ20170306154045928 and the Chinese National Science Foundation under Grant no. 51705430.

References

- [1] K. Tao, L. Tang, J. Wu, S. W. Lye, H. Chang, and J. Miao, "Investigation of Multimodal Electret-Based MEMS Energy Harvester With Impact-Induced Nonlinearity," *Journal of Microelectromechanical Systems*, vol. 27, no. 2, pp. 276–288, 2018.
- [2] K. Tao, J. Wu, L. Tang et al., "A novel two-degree-of-freedom MEMS electromagnetic vibration energy harvester," *Journal of Micromechanics and Microengineering*, vol. 26, no. 3, Article ID 035020, 2016.
- [3] K. Tao, J. Wu, L. Tang, L. Hu, S. W. Lye, and J. Miao, "Enhanced electrostatic vibrational energy harvesting using integrated opposite-charged electrets," *Journal of Micromechanics and Microengineering*, vol. 27, no. 4, p. 044002, 2017.
- [4] J. Yang, J. Zhong, and H. Chang, "A Closed-Loop Mode-Localized Accelerometer," *Journal of Microelectromechanical Systems*, vol. 27, no. 2, pp. 210–217, 2018.
- [5] M. S. Weinberg and A. Kourepenis, "Error sources in in-plane silicon tuning-fork MEMS gyroscopes," *Journal of Microelectromechanical Systems*, vol. 15, no. 3, pp. 479–491, 2006.
- [6] A. Walther, C. Le Blanc, N. Delorme, Y. Deimerly, R. Anciant, and J. Willemin, "Bias contributions in a MEMS tuning fork gyroscope," *Journal of Microelectromechanical Systems*, vol. 22, no. 2, Article ID 6342888, pp. 303–308, 2013.
- [7] K. Liu, W. Zhang, W. Chen et al., "The development of micro-gyroscope technology," *Journal of Micromechanics and Microengineering*, vol. 19, no. 11, Article ID 113001, 2009.
- [8] Q. Shen, H. Li, Y. Hao, W. Yuan, and H. Chang, "Bias Contribution Modeling for a Symmetrical Micromachined Coriolis Vibratory Gyroscope," *IEEE Sensors Journal*, vol. 16, no. 3, pp. 723–733, 2016.
- [9] D. Chen, X. Liu, H. Zhang et al., "A Rotational Gyroscope with a Water-Film Bearing Based on Magnetic Self-Restoring Effect," *Sensors*, vol. 18, no. 2, p. 415, 2018.
- [10] D. Chen, X. Liu, H. Zhang et al., "Friction reduction for a rotational gyroscope with mechanical support by fabrication of a biomimetic superhydrophobic surface on a ball-disk shaped rotor and the application of a water film bearing," *Micromachines*, vol. 8, no. 7, article no. 223, 2017.
- [11] H. Li, X. Liu, W. Chen, and H. Zhang, "A miniaturized two-DOF rotational gyro with a ball-joint supported permanent magnet rotor," *Applied Physics Letters*, vol. 109, no. 1, Article ID 013503, 2016.
- [12] H. Cao and H. Li, "Investigation of a vacuum packaged MEMS gyroscope architecture's temperature robustness," *International*

- Journal of Applied Electromagnetics and Mechanics*, vol. 41, no. 4, pp. 495–506, 2013.
- [13] A. A. Trusov, I. P. Prikhodko, S. A. Zotov, A. R. Schofield, and A. M. Shkel, “Ultra-high Q silicon gyroscopes with interchangeable rate and whole angle modes of operation,” in *Proceedings of the 2010 Ninth IEEE Sensors Conference (SENSORS 2010)*, pp. 864–867, Kona, HI, November 2010.
 - [14] A. A. Trusov, A. R. Schofield, and A. M. Shkel, “Vacuum Packaged Silicon MEMS Gyroscope with Q-Factor Above 0.5 Million,” *Additional Conferences (Device Packaging, HiTEC, HiTEN, & CICMT)*, vol. 2010, no. DPC, pp. 001335–001359, 2010.
 - [15] D. Senkal, S. Askari, M. J. Ahamed et al., “100K Q-factor toroidal ring gyroscope implemented in wafer-level epitaxial silicon encapsulation process,” in *Proceedings of the 2014 IEEE 27th International Conference on Micro Electro Mechanical Systems (MEMS)*, pp. 24–27, San Francisco, CA, USA, January 2014.
 - [16] I. P. Prikhodko, A. A. Trusov, and A. M. Shkel, “North-finding with 0.004 radian precision using a silicon MEMS quadruple mass gyroscope with Q-factor of 1 million,” in *Proceedings of the 2012 IEEE 25th International Conference on Micro Electro Mechanical Systems (MEMS)*, pp. 164–167, Paris, France, January 2012.
 - [17] C. Zener, “Internal friction in solids. I. Theory of internal friction in reeds,” *Physical Review A: Atomic, Molecular and Optical Physics*, vol. 52, no. 3, pp. 230–235, 1937.
 - [18] C. Zener, “Internal friction in solids II. General theory of thermoelastic internal friction,” *Physical Review A: Atomic, Molecular and Optical Physics*, vol. 53, no. 1, pp. 90–99, 1938.
 - [19] Y. Xu, R. Wang, S. K. Durgam, Z. Hao, and L. Vahala, “Numerical models and experimental investigation of energy loss mechanisms in SOI-based tuning-fork gyroscopes,” *Sensors and Actuators A: Physical*, vol. 152, no. 1, pp. 63–74, 2009.
 - [20] S. Nitzan, C. H. Ahn, T. Su et al., “Epitaxially-encapsulated polysilicon disk resonator gyroscope,” in *Proceedings of the 2013 IEEE 26th International Conference on Micro Electro Mechanical Systems (MEMS)*, pp. 625–628, Taipei, Taiwan, January 2013.
 - [21] S. Ghaffari, E. J. Ng, C. H. Ahn et al., “Accurate modeling of quality factor behavior of complex silicon MEMS resonators,” *Journal of Microelectromechanical Systems*, vol. 24, no. 2, Article ID 6994789, pp. 276–288, 2015.
 - [22] B. Kim, M. A. Hopcroft, R. N. Candler et al., “Temperature dependence of quality factor in MEMS resonators,” *Journal of Microelectromechanical Systems*, vol. 17, no. 3, pp. 755–766, 2008.
 - [23] C. M. Jha, M. A. Hopcroft, S. A. Chandorkar et al., “Thermal isolation of encapsulated MEMS resonators,” *Journal of Microelectromechanical Systems*, vol. 17, no. 1, pp. 175–184, 2008.
 - [24] E. J. Ng, H. K. Lee, C. H. Ahn, R. Melamud, and T. W. Kenny, “Stability of silicon microelectromechanical systems resonant thermometers,” *IEEE Sensors Journal*, vol. 13, no. 3, pp. 987–993, 2013.
 - [25] Y. Chen, E. J. Ng, Y. Yang, C. H. Ahn, I. Flader, and T. W. Kenny, “In-situ ovenization of Lamé-mode silicon resonators for temperature compensation,” in *Proceedings of the 2015 28th IEEE International Conference on Micro Electro Mechanical Systems (MEMS)*, pp. 809–812, Estoril, Portugal, January 2015.
 - [26] I. P. Prikhodko, B. R. Simon, G. Sharma, S. A. Zotov, A. A. Trusov, and A. M. Shkel, “High and moderate-level vacuum packaging of vibratory MEMS,” in *Proceedings of the 46th Annual IMAPS International Symposium on Microelectronics, IMAPS 2013*, pp. 705–710, usa, October 2013.
 - [27] A. A. Trusov, A. R. Schofield, and A. M. Shkel, “Micromachined rate gyroscope architecture with ultra-high quality factor and improved mode ordering,” *Sensors and Actuators A: Physical*, vol. 165, no. 1, pp. 26–34, 2011.
 - [28] A. R. Schofield, A. A. Trusov, and A. M. Shkel, “Versatile vacuum packaging for experimental study of resonant MEMS,” in *Proceedings of the 2010 IEEE 23rd International Conference on Micro Electro Mechanical Systems (MEMS)*, pp. 516–519, Wanchai, Hong Kong, China, January 2010.
 - [29] B. Chen, V. N. Sekhar, C. Jin et al., “Low-loss broadband package platform with surface passivation and TSV for wafer-level packaging of RF-MEMS devices,” *IEEE Transactions on Components, Packaging, and Manufacturing Technology*, vol. 3, no. 9, pp. 1443–1452, 2013.
 - [30] H. Kuisma, “Glass isolated TSVs for MEMS,” in *Proceedings of the 5th Electronics System-Integration Technology Conference, ESTC 2014*, fin, September 2014.
 - [31] C. H. Liu, H. D. K. H. Chang et al., “Adaptable and integrated packaging platform for mems-based combo sensors utilizing innovative,” in *Proceedings of the Electronic Components & Technology Conference, IEEE 63rd*, pp. 1675–1681, 2013.
 - [32] X. Xi, X. Wu, Y. Zhang, X. Zhou, X. Wu, and Y. Wu, “A study on Q factor of the trimmed resonator for vibratory cupped gyroscopes,” *Sensors and Actuators A: Physical*, vol. 218, pp. 23–32, 2014.
 - [33] J.-H. Kim and J.-H. Kim, “Thermoelastic damping effect of the micro-ring resonator with irregular mass and stiffness,” *Journal of Sound and Vibration*, vol. 369, pp. 168–177, 2016.
 - [34] Z. Hao, Y. Xu, and S. K. Durgam, “A thermal-energy method for calculating thermoelastic damping in micromechanical resonators,” *Journal of Sound and Vibration*, vol. 322, no. 4–5, pp. 870–882, 2009.
 - [35] R. N. Candler, A. Duwel, M. Varghese et al., “Impact of geometry on thermoelastic dissipation in micromechanical resonant beams,” *Journal of Microelectromechanical Systems*, vol. 15, no. 4, pp. 927–934, 2006.
 - [36] J. Bartolomé, A. Cremades, and J. Piqueras, “High quality factor indium oxide mechanical microresonators,” *Applied Physics Letters*, vol. 107, no. 19, Article ID 191910, 2015.
 - [37] A. Sampaolo, P. Patimisco, L. Dong et al., “Quartz-enhanced photoacoustic spectroscopy exploiting tuning fork overtone modes,” *Applied Physics Letters*, vol. 107, no. 23, Article ID 231102, 2015.
 - [38] Y. Tao, J. M. Boss, B. A. Moores, and C. L. Degen, “Single-crystal diamond nanomechanical resonators with quality factors exceeding one million,” *Nature Communications*, vol. 5, article no. 3638, 2014.
 - [39] J. J. Bernstein, M. G. Bancu, J. M. Bauer et al., “High Q diamond hemispherical resonators: Fabrication and energy loss mechanisms,” *Journal of Micromechanics and Microengineering*, vol. 25, no. 8, Article ID 085006, 2015.
 - [40] O. Auciello, S. Pacheco, A. V. Sumant et al., “Are diamonds a MEMS’ best friend?” *IEEE Microwave Magazine*, vol. 8, no. 6, pp. 61–75, 2007.
 - [41] V. P. Adiga, A. V. Sumant, S. Suresh et al., “Mechanical stiffness and dissipation in ultrananocrystalline diamond microresonators,” *Physical Review B: Condensed Matter and Materials Physics*, vol. 79, no. 24, Article ID 245403, 2009.
 - [42] H. Najar, A. Thron, C. Yang et al., “Increased thermal conductivity polycrystalline diamond for low-dissipation micromechanical resonators,” in *Proceedings of the 27th IEEE International*

- Conference on Micro Electro Mechanical Systems, MEMS 2014*, pp. 628–631, usa, January 2014.
- [43] H. Najar, M.-L. Chan, H.-A. Yang, L. Lin, D. G. Cahill, and D. A. Horsley, “High quality factor nanocrystalline diamond micromechanical resonators limited by thermoelastic damping,” *Applied Physics Letters*, vol. 104, no. 15, Article ID 151903, 2014.
- [44] A. Gaidarzhy, M. Imboden, P. Mohanty, J. Rankin, and B. W. Sheldon, “High quality factor gigahertz frequencies in nanomechanical diamond resonators,” *Applied Physics Letters*, vol. 91, no. 20, Article ID 203503, 2007.
- [45] O. Auciello and A. V. Sumant, “Status review of the science and technology of ultrananocrystalline diamond (UNCD™) films and application to multifunctional devices,” *Diamond and Related Materials*, vol. 19, no. 7-9, pp. 699–718, 2010.
- [46] Z. Hao, A. Erbil, and F. Ayazi, “An analytical model for support loss in micromachined beam resonators with in-plane flexural vibrations,” *Sensors and Actuators A: Physical*, vol. 109, no. 1-2, pp. 156–164, 2003.
- [47] K. Y. Yasumura, T. D. Stowe, E. M. Chow et al., “Quality factors in micron- and submicron-thick cantilevers,” *Journal of Microelectromechanical Systems*, vol. 9, no. 1, pp. 117–125, 2000.
- [48] A. Frangi, A. Bugada, M. Martello, and P. Savadkoochi, “Validation of PML-based models for the evaluation of anchor dissipation in MEMS resonators,” *European Journal of Mechanics - A/Solids*, vol. 37, pp. 256–265, 2013.
- [49] V. Thakar and M. Rais-Zadeh, “Optimization of tether geometry to achieve low anchor loss in Lamé-mode resonators,” in *Proceedings of the 2013 Joint European Frequency and Time Forum and International Frequency Control Symposium, EFTF/IFC 2013*, pp. 129–132, cze, July 2013.
- [50] L. Khine and M. Palaniapan, “High-Q bulk-mode SOI square resonators with straight-beam anchors,” *Journal of Micromechanics and Microengineering*, vol. 19, no. 1, Article ID 015017, 2009.
- [51] J. E.-Y. Lee, J. Yan, and A. A. Seshia, “Study of lateral mode SOI-MEMS resonators for reduced anchor loss,” *Journal of Micromechanics and Microengineering*, vol. 21, no. 4, Article ID 045010, 2011.
- [52] P. An, Y. Zheng, S. Yan, C. Xue, W. Wang, and J. Liu, “High-Q microsphere resonators for angular velocity sensing in gyroscopes,” *Applied Physics Letters*, vol. 106, no. 6, Article ID 063504, 2015.
- [53] D. Saito, C. Yang, A. Heidari, H. Najar, L. Lin, and D. A. Horsley, “Microcrystalline diamond cylindrical resonators with quality-factor up to 0.5 million,” *Applied Physics Letters*, vol. 108, no. 5, Article ID 051904, 2016.
- [54] D. Senkal, M. J. Ahamed, A. A. Trusov, and A. M. Shkel, “Achieving sub-hz frequency symmetry in micro-glassblown wineglass resonators,” *Journal of Microelectromechanical Systems*, vol. 23, no. 1, Article ID 6651691, pp. 30–38, 2014.
- [55] Z. Hao and F. Ayazi, “Support loss in the radial bulk-mode vibrations of center-supported micromechanical disk resonators,” *Sensors and Actuators A: Physical*, vol. 134, no. 2, pp. 582–593, 2007.
- [56] A. D. Challoner, H. H. Ge, and J. Y. Liu, “Boeing Disc Resonator Gyroscope,” in *Proceedings of the 2014 IEEE/ION Position, Location and Navigation Symposium - PLANS 2014*, pp. 504–514, Monterey, CA, USA, May 2014.
- [57] C. H. Ahn, E. J. Ng, V. A. Hong et al., “Mode-matching of wineglass mode disk resonator gyroscope in (100) single crystal silicon,” *Journal of Microelectromechanical Systems*, vol. 24, no. 2, Article ID 6844857, pp. 343–350, 2015.
- [58] H. Chang, Y. Zhang, J. Xie, Z. Zhou, and W. Yuan, “Integrated behavior simulation and verification for a MEMS vibratory gyroscope using parametric model order reduction,” *Journal of Microelectromechanical Systems*, vol. 19, no. 2, Article ID 5393089, pp. 282–293, 2010.
- [59] H. Chang, J. Xie, Q. Fu, Q. Shen, and W. Yuan, “Micromachined inertial measurement unit fabricated by a SOI process with selective roughening under structures,” *Micro & Nano Letters*, vol. 6, no. 7, pp. 486–489, 2011.
- [60] J. Xie, Y. Hao, Q. Shen, H. Chang, and W. Yuan, “A dicing-free SOI process for MEMS devices based on the lag effect,” *Journal of Micromechanics and Microengineering*, vol. 23, no. 12, Article ID 125033, 2013.
- [61] J.-P. Berenger, “A perfectly matched layer for the absorption of electromagnetic waves,” *Journal of Computational Physics*, vol. 114, no. 2, pp. 185–200, 1994.
- [62] D. S. Bindel and S. Govindjee, “Elastic PMLs for resonator anchor loss simulation,” *International Journal for Numerical Methods in Engineering*, vol. 64, no. 6, pp. 789–818, 2005.
- [63] L. D. Sorenson, *Design and analysis of micro-electromechanical resonators with ultra-low dissipation*, Department of Electrical and Computer Engineering, Georgia Institute of Technology, 2013.
- [64] T. Veijola and M. Turowski, “Compact damping models for laterally moving microstructures with gas-rarefaction effects,” *Journal of Microelectromechanical Systems*, vol. 10, no. 2, pp. 263–273, 2001.
- [65] J. Z. Lin, X. D. Ruan, B. G. Chen et al., *Fluid Mechanics*, Tsinghua University Press, Beijing, 2005.

